An integrated hardware-in-loop approach for Lithium-ion batteries with single phase mechanically pumped fluid loop under space environment

Y Bi[1,2]*, M Yu[1], H Xu[2], A Wang[2], L Gao[2], X Zhang[2], B Feng[2], J Wang[2]

1. Department of Electrical Engineering, Hebei Vocational University of Technology and Engineering, Xingtai, 054035, China

2. Advanced Research Center of Thermal and New Energy Technologies, Hebei Vocational University of Technology and Engineering; Hebei Key Laboratory of Man-machine Environment Thermal Control Technology and Equipment, Xingtai, 054035, China

ABSTRACT

The excellent temperature characteristics of space Li-ion batteries can effectively improve the on-orbit operation, reduce temperature fluctuation range and improve reliability. In this paper, the hardware-in-the-loop approach is used for simulation and experiment. This method cannot only effectively test the thermal management system of space battery, but also simulate the characteristics of the system in real-time to save high experimental costs. The results show that when the temperature of the inlet working fluid increases, the surface temperature increases significantly, with a maximum temperature difference of 4.9 °C. At the same time, the steady state settling time of the surface temperature also increases. When the flow rate of the inlet working fluid increases, the surface temperature decreases significantly. The maximum temperature difference is 3.9°C, and the steady state settling time of the surface temperature is greatly shortened. As the thermal load increases, the surface temperature of the battery increases obviously. The maximum temperature difference is 3.9°C, and the steady state settling time of the surface temperature is long. When the cycle is the same and the charge/discharge time is different, the longer the discharge time, the faster the surface temperature increases, up to 34%.

1. INTRODUCTION

Lithium-ion battery has been proven to be an essential energy storage device in space stations due to its eco-friendliness, large single voltage, high power-to-weight ratio, wide operating temperature ranges (-30°C ~+60°C), and long cycling life [1-3]. The performance of space Li-ion battery depends largely on its operating temperature and temperature uniformity [4-5]. Improper operating temperature may lead to lower charging efficiency and cycling life of the battery [6-7]. Moreover, due to the uneven temperature distribution of a single battery cell, the battery capacity will decrease [8].

*Corresponding Author: binyang012@126.com

The thermal management system (TMS) aims to effectively improve the performance of the battery through air, liquid and phase change materials with different cooling technologies [9-10]. How to accurately obtain the temperature characteristics of lithium-ion batteries on the space station through scientific, effective and convenient methods is of great significance for evaluating TMS performance, optimal design of TMS core components and further developing other more effective thermal control strategies.

Traditionally, there are two main methods for TMS verification and performance evaluation of lithium-ion batteries: numerical simulation method and all-physical experimental method. Numerical studies of the thermal control performance of TMS using finite element analysis (FEA) method and computational fluid dynamics (CFD) method has attracted extensive attention. An effective CFD simulation of an integrated TMS with a designed forced air and liquid plate was carried out to improve the temperature stability and uniformity of batteries in space [11]. The thermal performance of the battery pack was analyzed by CFD method, and the parameters of the microchannel cold plate were optimized [12]. The effect of liquid cold plates with various heat transfer enhancement fins on the heat dissipation capacity of the battery was analyzed by CFD [13]. FEA method has also been used to calculate the thermal characteristics of cylindrical Lithium-ion power batteries with microchannel liquid-cooled cylinders [14-15]. In addition, other numerical approaches, such as lumped parameter model (LPM) methods have also been used in TMS design for Lithium-ion batteries [16]. Compared with the experimental method, the numerical simulation method is undoubtedly a more economical method. However, validity of the simulation results mainly depends on detailed mathematical models, perfect geometrical meshes and better initial values. Furthermore, a lot of patience is essential for geometric modeling and meshing.

In terms of physical experiments, a lot of work has also been made to improve the performance of ground-based TMS lithium-ion batteries. Compared with numerical simulations, the experimental methods can be more reliable, trustable and accurate. Most studies have been devoted to validating liquid cooled lithium-ion batteries TMS. Li et al. investigated the thermal characteristics of a battery TMS using a water-cooling method in the dynamic cycling of the battery pack through a test bench composed of a battery pack, motor peristaltic tubing pump, battery circulator, thermocouples and control computer [17]. Chen et al. conducted a heat-dissipation experiment on a liquid-cooled battery module device to measure the cooling effect and fluid pressure of different optimized design plans [18]. Malik et al. evaluated the thermal characteristics of lithium-ion battery packages under the actual driving cycles of constant current discharge rates and liquid cooling [19]. Specially designed experiments were carried out for the coupled composite liquid cooling and phase change material (PCM) TMS of a lithium-ion battery pack in continuous operations under different ambient environments [20]. A battery module, consisting of 3×5 cells immersed in a paraffin-copper composite enclosed in an aluminum shell, has been experimentally tested by external single and double-sided liquid cooling [21]. Significant progress has been made in the design and testing of lithium-ion batteries TMS. However, the research of ground-based full physical experiment strongly requires actual physical equipment, such as vacuum chambers and cooling systems, to simulate the space environment.

The hardware-in-loop (HIL) approach [22-23] combines the advantages of experimental and numerical methods and becomes a promising candidate method for the study of thermal behaviors of batteries under different TMSs. This HIL-based experimental simulation has been applied to solve various engineering issues, including the integrated velocity and force control of robot contact dynamics simulation on satellites [24], design and verification of bypass valve actuation systems [25], and real-time verification of electrical vehicle closed-loop control systems [26]. Li et al. used the HIL method to predict and simulate the temperature of permanent magnet synchronous machines (PMSMs) thermal boundary accurately and flexibly [27]. Han et al. adopted the hardware-in-loop simulation (HILS) to study the thermal and static characteristics of hydrogen fuel cell vehicles under changing driving conditions [28]. It is proved that the HIL-based method can be efficiently applied to the thermal analysis of hydrothermal coupling system.

In this paper, the hardware-in-the-loop method is used to study the steady-state characteristics and surface temperature stabilization time of space batteries under three disturbances: inlet working fluid temperature, flow rate and heat load. The temperature characteristics provide an important reference for the on-orbit management of space lithium batteries.

2. SYSTEM DESCRIPTION AND MODELING

2.1. Integrated HIL based system

The Integrated HIL-based system includes an equivalent battery and power supply controller (PCU) heat source simulation part, fluid circuit part, and a measurement and control part, as shown in Figure 1. Heat collection, transfer and dissipation are integral components of the spacecraft active thermal control systems. In this system, the heat collection link mainly includes the equivalent battery and the simulated PCU heat source. The equivalent battery and PCU components of the simulated heat source are closely attached to the cold plate, which absorbs the heat transferred by the heat source load through thermal conduction and exchanges the heat to the fluid network. After the heat exchange in the cold plate, the waste heat enters the transmission link, which is responsible for transferring the heat to the heat dissipation link. The heat dissipation link mainly includes valves, micromechanical pumps and fluid pipelines. The micromechanical pump is a controllable execution part, and its speed is adjusted by driving voltage control to regulate the flow of working medium and temperature. Finally, the heat enters the exhaust link after the transmission. The core component of the heat dissipation segment is the heat exchanger, which absorbs the heat from the fluid network and dissipates it into the external environment.

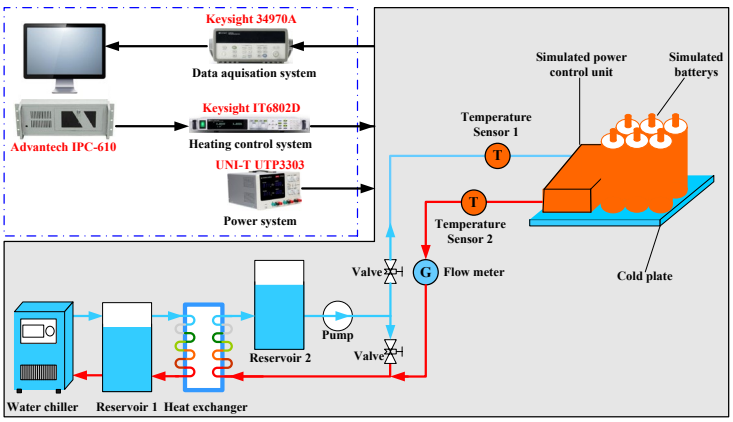

Figure 1: Single phase mechanically pumped fluid loop (SPMPFL) for thermal management of space Lithium-ion batteries

2.2. Description of heat source simulation components

The equivalent battery consists of four parts: outer cylindrical brass ring, PVC ring tube, nickel-chromium heating wire and paraffin, as shown in Figure 2(a) and 2(b). The outer cylindrical copper ring has an outer diameter of 54 mm, a wall thickness of 3 mm and a height of 174 mm. It is integrated with the lower cover plate of the cylinder with a diameter of 54 mm and a height of 3 mm.

The upper cover plate has a diameter of 54mm, a height of 3mm, and two openings with a diameter of 3mm to facilitate the passage of the nickel-chromium (Ni-Cr) heating wire and the lead wire of the temperature sensor. The Ni-Cr heating wire has a length of1.5m long and a diameter of 2mm. The diameter of the PVC ring pipe has a diameter of48mm, a wall thickness of 2mm, and a height of 163mm. The height and diameter of the Paraffin are 163 and 44 mm, respectively. The paraffin is put into the PVC pipe, and the nickel-chromium heating wire is wound on the PVC pipe, and then put together in the outer cylindrical brass ring. The equivalent power supply controller (PCU) is made of nickel-chrome alloy heating wire wound on a plastic cage support, as shown in Figure 3.

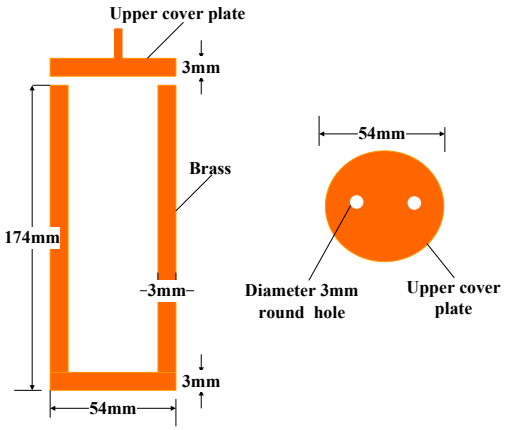

(a)

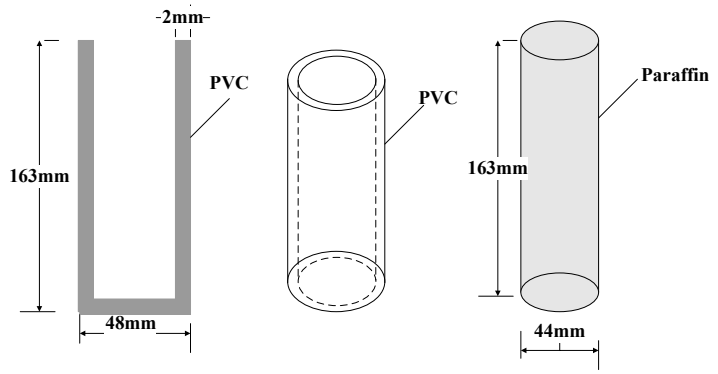

(b)

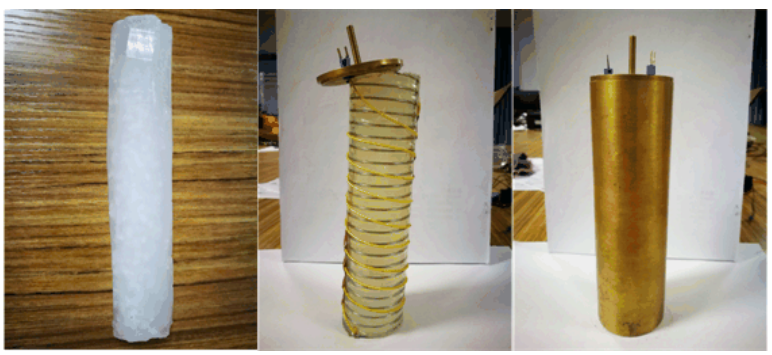

(c)

Figure 2: Schematic diagram of the equivalent battery. (a) Structural dimension of the cylindrical copper shell; (b) size and layout of composite filler materials; (c) the test equivalent battery cell

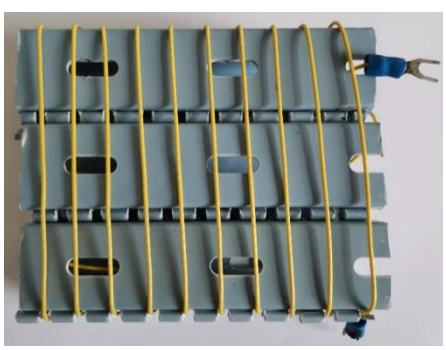

Figure 3: Simulation of the equivalent power control unit

The equivalent battery ratio is as follows:

$$cm = \sum c_i \, m_i \tag{1}$$

where, c is the specific heat capacity of actual cell ($J/(kg \cdot K)$), $m$is the mass of actual cell (kg); $c_i$is the specific heat capacity of each part of the material of the equivalent cell ($J/(kg \cdot K)$), and m_i is the mass of each part of the equivalent cell (kg). The thermo-physical parameters of the materials are shown in Table 1.

Table 1 Thermo-physical properties of the equivalent battery

Material	**Density (kg/m^3)**	**Specific heat capacity ($J/(kg \cdot K)$)**
Actual cell	2663	900
Brass	8440	377
Nickel-chrome alloy	8000	460.6
PVC	1350-1450	1045-1463
Paraffin	2650	900

2.3. Mathematical modeling

2.3.1. Temperature change equation of single battery

The state equation for temperature change of single battery is:

$$M_{b,i}C_{b,i}\frac{dT_{b,i}}{dt} = I(U_o - U - T_{b,i}\frac{dU_o}{dT}) - \frac{T_{b,i}-T_{cp}}{R_{b,i-cp}} - \varepsilon A\sigma(T_{b,i}^4 - T_a^4) \quad (2)$$

where, U is the electric voltage; U_o is the open circuit voltage; I is the electric current; ε is the efficiency of single battery; A is the area of single battery, and σ is the Boltzmann constant. $M_{b,i}C_{b,i}\frac{dT_{b,i}}{dt}$is the heat added by the battery per unit time; $I(U_o - U - T_{b,i}\frac{dU_o}{dT})$ is the heat produced by the battery per unit time, and $\frac{T_{b,i}-T_{cp}}{R_{b,i-cp}}$ is the heat absorbed by the cold plate. $\varepsilon A\sigma(T_{b,i}^4 - T_a^4)$ is the radiant heat, and $\frac{dU_o}{dT}$ represents the temperature coefficient of the battery open circuit voltage as a function of temperature.

2.3.2. Cold plate temperature equation

The state equation for the temperature of the cold plate is:

$$M_{cp}C_{cp}\frac{dT_{cp}}{dt} = \sum_i \frac{T_{b,i}-T_{cp}}{R_{b-cp}} - h_{cp}A_{cp}\varepsilon_{cp}(T_{cp} - T_f) \quad (3)$$

where T_b is the cell temperature; T_{cp} B is the cold plate temperature; R_{b-cp} is the thermal resistance between the cell and the cold plate;h_{cp} is the thermal convection coefficient between the cold plate and the working medium; $A_{cp}$is the equivalent heat convection area; ε_{cp} is the cold plate efficiency, $\varepsilon_{cp} = 1 - exp(-h_{cp}A_{cp}\eta_{cp}/V_f\rho_f C_f)$; η_{cp} is the fin efficiency; V_f is the volume flow of working medium, and $T_f$is the average temperature of the working fluid,$T_f = (T_{cp\_in} + T_{cp\_out})/2$.

3. EXPERIMENTAL RELATIONS

3.1. Experimental setup and principle

The experimental device mainly consists of three parts: the simulation battery and PCU heat source simulation part, the single-phase mechanical pump fluid circuit part, and the measurement and control part, as shown in Figure 4. Programmable DC regulated power supply (ITECH IT6502D) programming output is used to control the heating power of analog battery and PCU. The data acquisition instrument (Keysight 34972A+34901A) collects the inlet and outlet temperatures of the working medium and the battery temperature through a temperature transmitter (SBWZ-Pt100) and a temperature sensor (WZP-Pt100). The chiller (Nissan CW-1000A (1 hp cold and warm)) provides constant temperature working medium. The heat produced by the battery and PCU is simulated to taken away by the cold plate through thermal conduction, and then exchanged to the fluid network. The waste heat is then transferred to the heat exchanger and finally dissipated to the external environment.

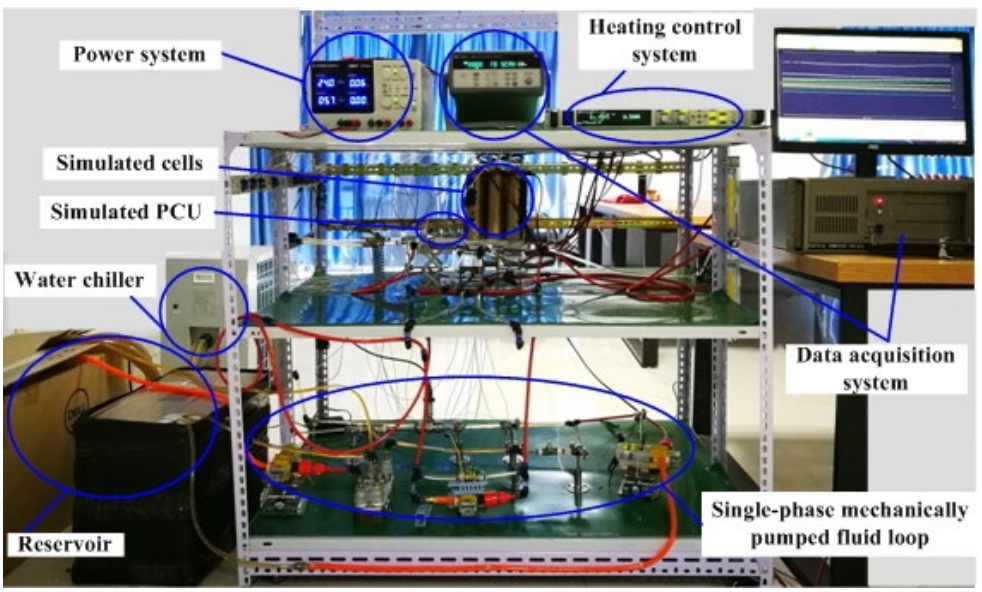

Figure 4: Photographic view of the verification testbeds

3.2. Experimental procedure and uncertainty analysis

3.2.1. Set of temperature sensors

The locations of the cold plate, equivalent battery, and temperature sensor are shown in Fig. 5(a) and 5(b), respectively. The three temperature sensors on the cold plate are G, H and I, respectively, and the inlet and outlet temperature sensors are J and K, respectively. Two temperature sensors are installed on the inside and outside of each battery to test the temperature changes of the battery during heating.

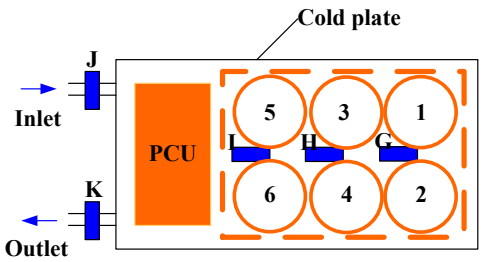

(a)

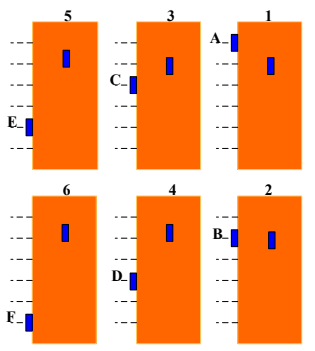

(b)

Figure 5: Installation of temperature sensors. (a) Top view of the cell array; (b) thermal resistance locations inside and on the outer wall of the battery

3.2.2. Experimental procedure

1). Turn on the cooler, the data acquisition instrument, the power supply, the programmable DC regulated power supply, the industrial computer, and the micromechanical pump, adjust the flow rate to a fixed value until the temperature contrast between the inlet and outlet is stable at 3-5°C.

2). Set the programmable DC regulated power supply to simulate the heating power during the battery discharge and charge.

3). Record the data.

Note that the ambient temperature remains constant during the experiment.

3.2.3. Uncertainty of measurement

Flow meter and temperature sensor have measurement errors. There are errors in the outlet temperature of the cooler, and there are changes in the laboratory temperature environment.

4. EXPERIMENTAL RESULTS AND DISCUSSIONS

4.1. Case I: Steady performance

The experiments are divided into 3 conditions. Condition I: Given a flow rate of 10L/h and a heat load of78.9W, the inlet temperature varies from 20°C to 10°C. Condition II: Given an inlet temperature of 20°C and a heat load of 78.9W, the flow rate varies from 10L/h to 6L/h. Condition III: Given a flow rate of 10 L/h and an inlet temperature of 20°C, the thermal load varies from 78.9W to 58.9W, shown as Table 2.

Table 2: Detailed designs of experimental parameters

Serial number	Working conditions	Disturbance
Condition I	flow rate 10L/h, heat load 78.9W	inlet temperature: 20℃, 15℃, 10℃
Condition II	inlet temperature 20℃, heat load 78.9W	flow rate: 10L/h, 8L/h, 6L/h
Condition III	flow rate 10L/h, inlet temperature 20℃	heat load: 78.9W, 68.9W, 58.9W

4.1.1 Temperature disturbance of inlet working fluid

Variation of the surface temperature with inlet working fluid temperature is shown in Figure 6. Due to different positions of sensors, the surface temperatures of the 6 simulated batteries are also different, while the increase is basically the same. When the inlet temperature of the lowest battery 6 is 10°C, the battery surface temperature is 27.3°C. When the inlet temperature is 20°C, the surface temperature of the battery is 32.2°C. The temperature difference is 4.9°C, and the slope of the curve is 0.49. When the inlet temperature of the highest battery 3 is 10°C, the surface temperature of the battery is 36.7°C. When the inlet value is 20°C, the battery surface temperature is 41.6°C. The temperature difference is 4.9°C, and the slope of the curve is 0.49.It indicates that as the inlet working fluid temperature increases, the steady-state temperature of the surface also increases due to the reduction of the heat taken away by the cold plate.

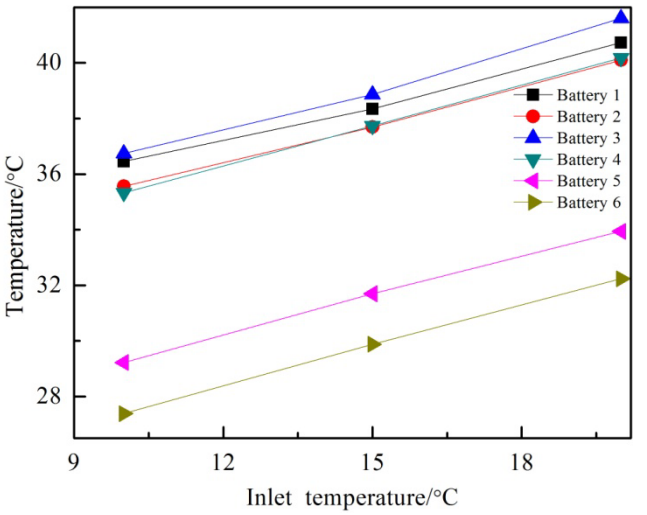

Figure 6: The battery surface temperatures under different inlet conditions

The temperature of the inlet working fluid is different, and the steady state settling time of the surface temperature is shown in Figure 7. As the inlet working fluid temperature increases, the steady state settling time of the battery surface temperature also increases. When the inlet temperature of the battery 1 is 10°C, the steady-state settling time of the surface temperature is 3660s; when it is 20°C, the steady-state settling time of the surface temperature is 3960s.

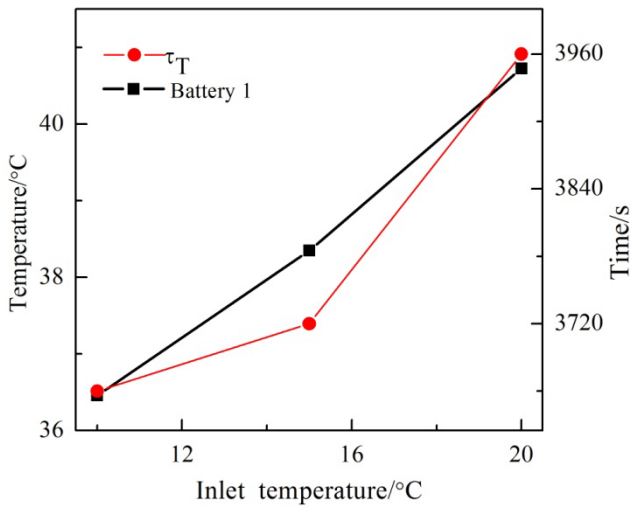

Figure 7: Steady-state establishment time of surface temperature under different inlet conditions

4.1.2 Volumetric flow rate disturbance

The change of the surface temperature with inlet working fluid flow rate is shown in Figure 8. For the lowest temperature battery 6, when the inlet working fluid flow rate is 6 L/h, the surface temperature of the battery is 36.5 °C; when it is 10 L/h, the surface temperature of the battery is 32.6 °C. The temperature difference is 3.9 °C, and the slope of the curve is 0.975. For the highest temperature battery 3, when the inlet working fluid flow rate is 6L/h, the surface temperature of the battery is 46.0 °C; when it is 10L/h, the surface temperature of the battery is 42.6°C. The temperature contrast is 3.4°C, and the slope of the curve is 0.85. It can be seen that as the inlet working fluid flow rate increases, the steady-state temperature of the surface decreases. The reason is that as the flow rate increases, the heat absorbed by the cold plate increases, and the heat dissipation effect is optimal.

The flow rate of the inlet working fluid is different, and the steady state settling time curve of the surface temperature is shown in Figure 9. As the inlet working fluid flow rate increases, the steady-state establishment time of the battery surface temperature is short. When the inlet working fluid flow rate of the battery 1 is 6L/h, the steady-state establishment time of the surface temperature is the 2940s; when it is 10L/h, the steady-state establishment time of the surface temperature is 2340s.

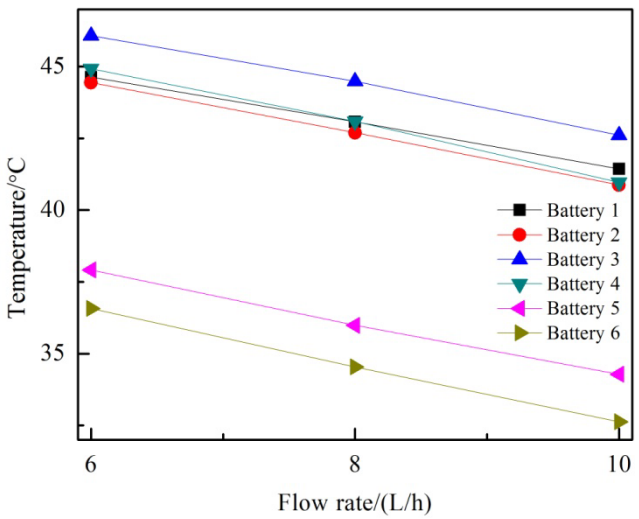

Figure 8: Surface temperature of the battery at different flow rates

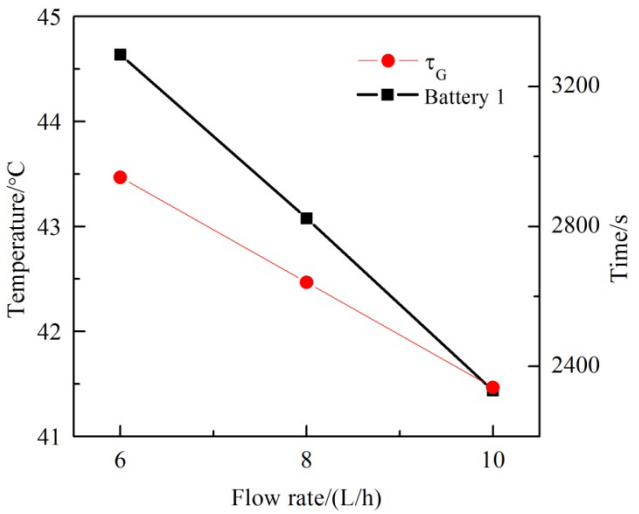

Figure 9: Steady-state establishment time of surface temperature at different flow rates

4.1.3. Thermal load disturbance

Variation of the surface temperature with thermal load is shown in Figure10. The lowest temperature battery 6 has a surface temperature of 30.0° C when the thermal load is 58.9 W. When the thermal load is 78.9W, the surface temperature of the battery is 32.1°C. The temperature difference is 3.9°C, and the slope of the curve is 0.105.

The highest temperature battery 3 has a surface temperature of 37.9°C when the thermal load is 58.9W. When the thermal load is 78.9W, the battery surface temperature is 41.8°C. The temperature difference is 3.9°C, and the slope of the curve is 0.105. Consequently, as the thermal load increases, the steady-state temperature of the surface increases accordingly. The heat produced by the battery directly affects the battery temperature. As the heat load increases, the surface temperature increases accordingly.

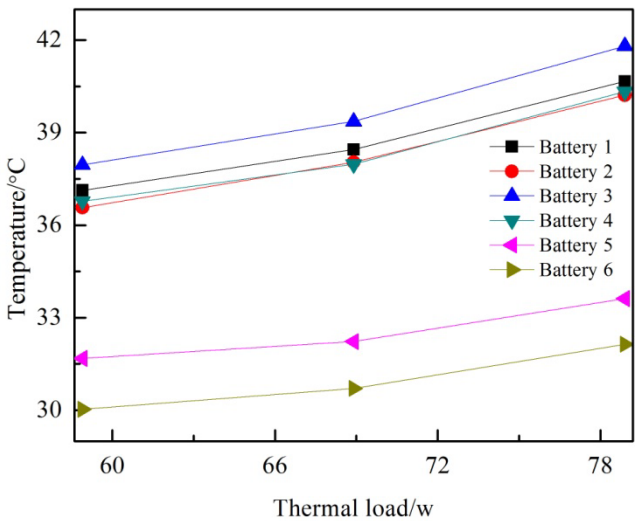

Figure 10: Surface temperature of the battery at different thermal loads

For different thermal loads, the steady-state establishment time of the surface temperature is shown in Figure 11. As the thermal load increases, the steady-state establishment time of the surface temperature becomes longer. When the thermal load of battery 1 is 58.9W, the steady-state establishment time of the surface temperature is 3180s. When the thermal load is 78.9W, the steady-state establishment time of the surface temperature is 4020s.

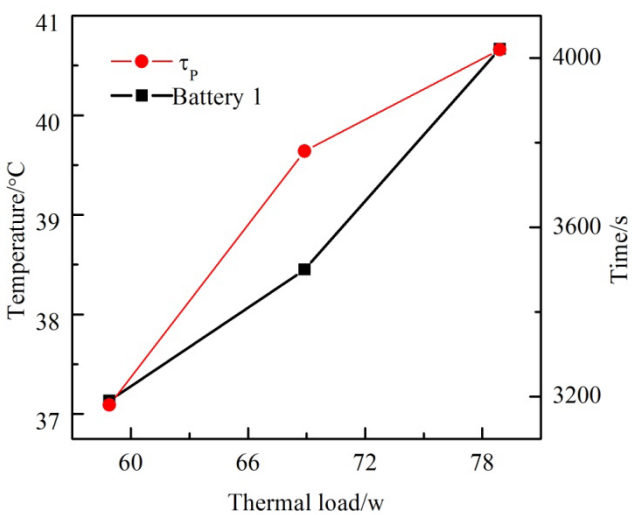

Figure 11: Steady-state establishment time of the battery surface temperature at different thermal loads

4.2. Case II: Cyclical characteristics

The experimental conditions are divided into two types. The total cycle of working condition 1 is fixed at 180 min, and the charge/discharge time is different. In condition 2, the discharge time is fixed at 10 min, and the total cycle and charging time change as shown in Table 3.

Table 3: Detailed design of experimental parameters

Serial number	Cycle/min	Charging time /min	Discharge time /min
	180	170	10
Condition 1	180	130	50
	180	90	90
	60	50	10
Condition 2	120	110	10
	180	170	10

4.2.1. Surface temperature of the battery changes with charge/discharge time

Figure 12 (a), (b), and (c) show the change in surface temperature with different charge/discharge cycles. During the discharging, battery 3 has the highest temperature and battery 6 has the lowest temperature, as shown in Table 4. Under the same cycle and charge/discharge time, the surface temperature of the same battery has little change. When the cycle is the same and the charge/discharge time is different, as the work cycle of the discharging time increases by 22%, the battery surface temperature increases significantly, up to 34%. This is because when the space lithium-ion battery is charged during the work cycle, the PCU heats up, while the battery does not. When discharging, the PCU and battery will heat up (the heat produced by the PCU during charging is greater than that during discharging). The longer the discharge time, the more heat will be discharged. During the charging process, battery 5 has the highest temperature, and battery 2 has the lowest temperature. Since the bottom of the battery is close to the cold plate, the heat dissipates quickly. For the same battery, the temperature of the upper part is higher than that of the lower part.

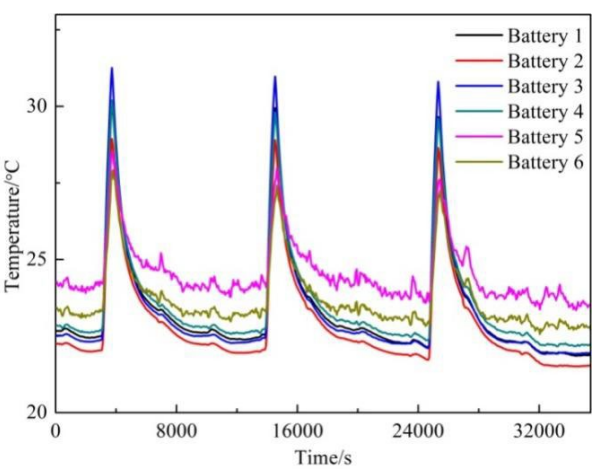

(a) 170min charge, 10min discharge

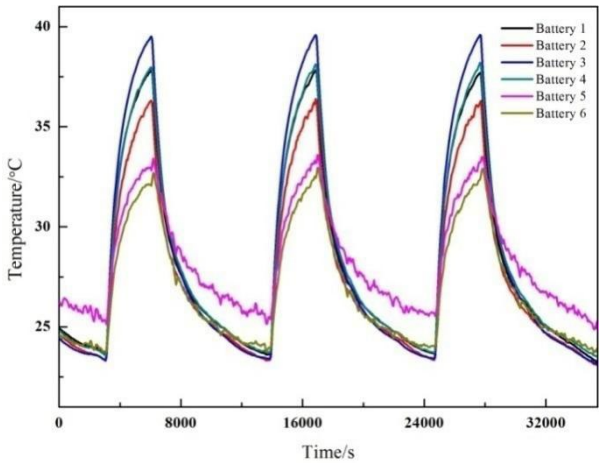

(b) 130min charge, 50min discharge

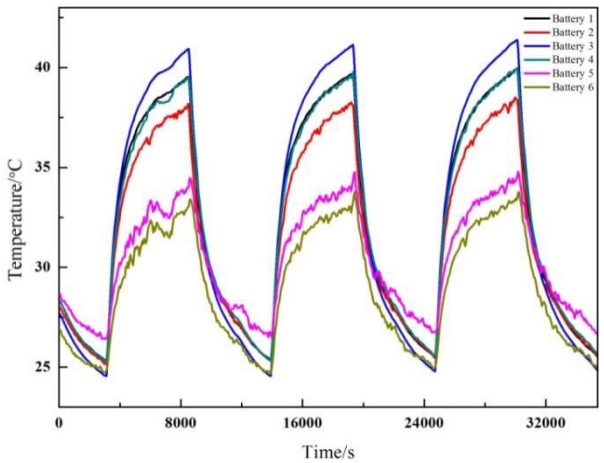

(c) 90min charge, 90min discharge

Figure 12: Surface temperature variation of the battery with different charge/discharge cycles

Table 4: Maximum and minimum surface temperatures of the battery for case 1

Battery	Charge 170min discharge 10min/°C			Charge 130min discharge 50min/°C			Charge 90min discharge 90min/°C		
Battery3	31.26	30.98	30.81	39.52	39.59	39.59	40.94	41.15	41.39
Battery6	27.92	27.11	27.25	32.71	32.96	32.92	33.42	33.79	33.78

4.2.2. Surface temperature of the battery varies with total number of cycles and charging time

The variation of surface temperature with different total cycles and charging time is shown in Figure 13(a), (b), and (c). During the discharging process, battery 3 has the highest temperature, and battery 6 has the lowest temperature, shown as Table 5. This indicates that the total cycle is different, and the discharge time is the same, and the surface temperature has little change.

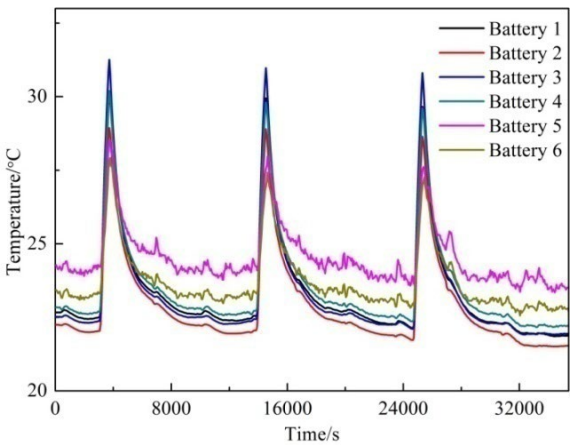

(a) 170min charge, 10min discharge

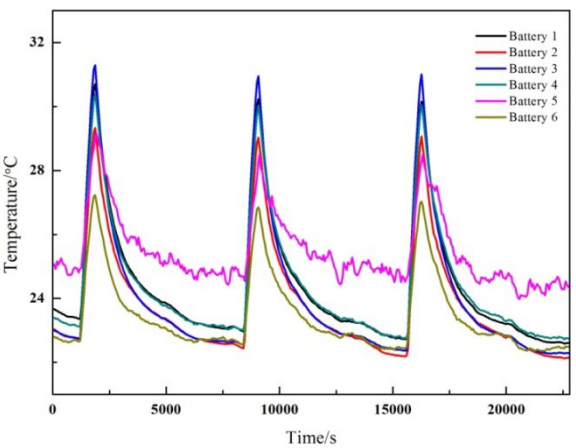

(b) 110min charge, 10min discharge

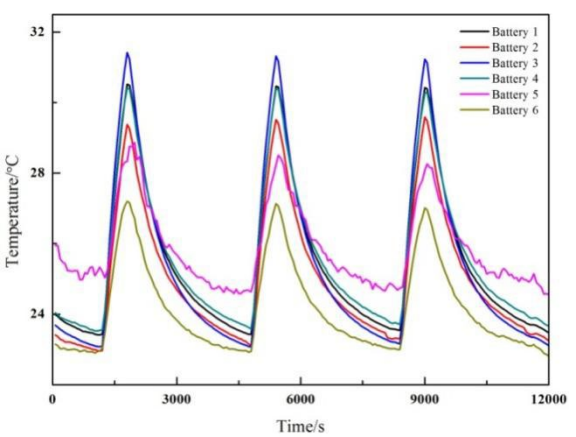

(c) 50min charge, 10min discharge

Figure 13 Surface temperature variation of the battery at different total cycles and charging times

Table 5 Maximum and minimum surface temperature of the battery for case 2

Battery	Charge 170min discharge 10min/°C			Charge 110min discharge 10min/°C			Charge 50min discharge 10min/°C		
Battery 3	31.26	30.98	30.81	31.30	30.95	31.01	31.42	31.32	31.23
Battery 6	27.92	27.11	27.25	27.23	26.85	27.03	27.20	27.14	27.01

5. CONCLUSIONS

Temperature is the main factor impacting the work performance, service life and reliability of space lithium battery. The temperature of lithium battery is mainly affected by the ambient temperature, thermal management system, and the reaction heat, ohmic heat, and polarization heat generated by the electrochemical reaction during charging/discharging. When the heat is too high and cannot dissipates in time, the performance of the battery will deteriorate, the life will be shortened, and even the incalculable loss will be caused. Here the steady-state characteristics of the temperature of space lithium-ion battery under the three disturbances of inlet working fluid temperature, flow rate and thermal load are analyzed, as well as the unsteady fluctuation law of the battery temperature caused by the periodic thermal load of charge/discharge. Conclusions are as follows:

1) Under low inlet working fluid temperature and large flow rate, the surface temperature is low, the steady-state establishment time is short, and the stability is optimal.
2) As the thermal load increases, the surface temperature increases significantly, and the steady state settling time is long. To ensure the reliability and stability of the battery, the heat generated by the battery should be maintained as small as possible.
3) When the cycle is the same and the charge/discharge time is different, as the discharge time increases, the surface temperature increases significantly, and the time for the temperature to peak increases gradually. This is because when the space battery is charged during the work cycle, PCU will heat up, while the battery will not. During the discharging, the PCU and battery will heat up at the same time. The longer the discharge time, the greater the heat releases. During the charging process, the battery close to PCU will have high heat and high surface temperature. Since the bottom of the battery is close to the cold plate, the heat dissipates quickly. For the same battery, the temperature of the upper part is higher than that of the lower part. In this way, to make the space lithium-ion battery work better, the discharge time should be as short as possible.

AUTHOR CONTRIBUTIONS

Yanjun Bi: conceptualization; Huijuan Xu and Xin Zhang: methodology; Lijun Gao and Bingyin Feng: validation; Aobing Wang: formal analysis; Yanjun Bi: investigation; Yanjun Bi: writing—original draft preparation; Minli Yu and Junqiang Wang: writing—review and editing. All authors have read and agreed to the published version of the manuscript.

ACKNOWLEDGMENTS

This work was supported by the Natural Science Foundation of Hebei Province of China (No. E2021108007).

CONFLICTS OF INTEREST

The authors declared that there is no conflict of interest in this paper.

REFERENCES

[1] Walker, W., Yayathi, S., Shaw, J., & Ardebili, H., Thermo-electrochemical evaluation of lithium-ion batteries for space applications. Journal of Power Sources, 2015, 298: p. 217-227.

[2] Avanzini, G., de Angelis, E. L., & Giulietti, F., Optimal performance and sizing of a battery-powered aircraft. Aerospace Science and Technology, 2016, 59: p. 132-144.

[3] Song, Y., Peng, Y., & Liu, D., Model-Based Health Diagnosis for Lithium-Ion Battery Pack in Space Applications. IEEE Transactions on Industrial Electronics,2021, 68(12): p. 12375-12384.

[4] Xin, Q., Xiao, J., Yang, T., Zhang, H., & Long, X. Thermal management of lithium-ion batteries under high ambient temperature and rapid discharging using composite PCM and liquid cooling. Applied Thermal Engineering, 2022, 210: p. 118230.

[5] Chang, G., Cui, X., Li, Y., & Ji, Y. Effects of reciprocating liquid flow battery thermal management system on thermal characteristics and uniformity of large lithium-ion battery pack. International Journal of Energy Research, 2020, 44(8): p. 6383-6395.

[6] Ouyang, D., He, Y., Chen, M., Liu, J., & Wang, J., Experimental study on the thermal behaviors of lithium-ion batteries under discharge and overcharge conditions. Journal of Thermal Analysis and Calorimetry, 2017, 132: p. 65-75.

[7] Dong, T., Peng, P., & Jiang, F., Numerical modeling and analysis of the thermal behavior of NCMlithium-ion batteries subjected to very high C-rate discharge/charge operations. International Journal of Heat and Mass Transfer, 2018, 117: p. 261-272.

[8] Panchal, S., Dincer, I., Agelin-Chaab, M., Fowler, M., & Fraser, R., Uneven temperature and voltage distributions due to rapid discharge rates and different boundary conditions for series-connected LiFePO4 batteries. International Communications in Heat and Mass Transfer, 2017, 81: p. 210-221.

[9] An, Z., Jia, L., Ding, Y., Dang, C., & Li, X., A review on Lithium-ion power battery thermal management technologies and thermal safety. Journal of Thermal Science, 2017, 26: p. 391-412.

[10] Deng, Y., Feng, C., Jiaqiang, E., Zhu, H., Chen, J., Wen, M., & Yin, H., Effects of different coolants and cooling strategies on the cooling performance of the power lithium ion battery system: A review. Applied Thermal Engineering, 2018, 142: p. 10-29.

[11] Wang, S., Li, Y., Li, Y. Z., Mao, Y., Zhang, Y., Guo, W., & Zhong, M., A forced gas cooling circle packaging with liquid cooling plate for the thermal management of Li-ion batteries under space environment. Applied Thermal Engineering, 2017, 123: p. 929-939.

[12] Wang, J., Lu, S., Wang, Y., Ni, Y., & Zhang, S., Novel investigation strategy for mini-channel liquid-cooledbattery thermal management system. International Journal of Energy Research, 2019, 44(3): p. 1971-1985.

[13] Fu, J., Xu, X., & Li, R., Battery module thermal management based on liquid coldplate with heat transfer enhanced fin. International Journal of Energy Research, 2019, 43(9): p. 4312-4321.

[14] Zhao, J., Rao, Z., & Li, Y., Thermal performance of mini-channel liquid cooled cylinder based battery thermal management for cylindrical lithium-ion power battery. Energy Conversion and Management, 2015, 103: p. 157-165.

[15] Kumbhar, P., Swaminathan, N., &Annabattula, R. K., Mesoscale analysis of Li-ion battery microstructure using sequential coupling of discrete element and finite element method. International Journal of Energy Research, 2022, 46(9): p. 12003-12025.
[16] Dan, D., Yao, C., Zhang, Y., Zhang, H., Zeng, Z., & Xu, X., Dynamic thermal behavior of micro heat pipe array-air cooling battery thermal management system based on thermal network model. Applied Thermal Engineering, 2019, 162: p. 114183.
[17] Li, K., Yan, J., Chen, H., & Wang, Q., Water cooling based strategy for lithium ion battery pack dynamic cycling for thermal management system. Applied Thermal Engineering, 2018, 132: p. 575-585.
[18] Chen, S., Peng, X., Bao, N., & Garg, A., A comprehensive analysis and optimization process for an integrated liquidcooling plate for a prismatic lithium-ion battery module. Applied Thermal Engineering, 2019, 156: p. 324-339.
[19] Malik, M., Dincer, I., Rosen, M. A., Mathew, M., & Fowler, M., Thermal and electrical performance evaluations of series connected Li-ion batteries in a pack with liquid cooling. Applied Thermal Engineering, vol. 129, pp. 472-481, 2018.
[20] Kong, D., Peng, R., Ping, P., Du, J., Chen, G., & Wen, J., A novel battery thermal management system coupling with PCM and optimized controllable liquid cooling for different ambient temperatures. Energy Conversion and Management, 2020, 204: p. 112280.
[21] Li, J., & Zhang, H., Thermal characteristics of power battery module with compositephase change material and external liquid cooling. International Journal of Heat and Mass Transfer, 2020, 156: p. 119820.
[22] Badar, J., Ali, S., Munir, H. M., Bhan, V., Bukhari, S. S. H., & Ro, J. S., Reconfigurable Power Quality Analyzer Applied to Hardware-in-Loop Test Bench. Energies, 2021, 14(16): p. 5134.
[23] Geddam, K. K., &Devaraj, E., Real Time Hardware-in-Loop Implementation of LLC Resonant Converter at Worst Operating Point Based on Time Domain Analysis. Energies, 2022, 15(10): p. 3634.
[24] He, J., Shen, M. J., Hybrid Force/Velocity Control for Simulating Contact Dynamics of Satellite Robots on a Hardware-in-the-Loop Simulator. IEEE Access, 2022, 10: p. 59277-59289.
[25] Pugi, L., Galardi, E., Carcasci, C., Rindi, A., & Lucchesi, N., Preliminary design and validation of a Real Time model for hardware in the loop testing of bypass valve actuation system. Energy Conversion and Management, 2015, 92: p. 366-384.
[26] Yan, Y., Liu, C., Ma, X., & Zhang, Y., Hardware-in-loop real-time simulation of electrical vehicle using multi-simulation platform based on data fusion approach. International Journal of Distributed Sensor Networks, 2019, 15(4): p. 1550147719841493.
[27] Li, Y.Z., Zhu, S.J., Li, Y., Lu, Q., Temperature prediction and thermal boundary simulation using hardware-in-loop method for permanent magnet synchronous motors. IEEE/ASME Transactions on Mechatronics, 2016, 21(1): p. 276-287.
[28] Han, J., Han, J., & Yu, S., Emulation of Thermal Energy Generation of Fuel Cell Stack via Hardware in Loop Simulation. Transactions of the Korean Society of Mechanical Engineers B, 2018, 42(11): p. 735-744.